

Flow Statistics and Noise of Ideally Expanded Supersonic Rectangular and Circular Jets

Kamal Viswanath,* Ryan Johnson,† Andrew Corrigan,‡ and K. Kailasanath§

Naval Research Laboratory, Washington, D.C. 20375

and

Pablo Mora,¶ Florian Baier,** and Ephraim Gutmark††

University of Cincinnati, Cincinnati, Ohio 45221

DOI: 10.2514/1.J055717

Simulations of an ideally expanded supersonic jet for two operating temperatures are conducted with a low aspect ratio of two rectangular nozzle, and an equivalent diameter circular nozzle of the same design Mach number. The emphasis is on accurately resolving the near-field data, capturing the far-field acoustics, and examining the flow asymmetry of the rectangular jets. The simulated acoustic data of the cold and heated jets are validated against experimentally recorded sound-pressure-level spectra with very good agreement. Rectangular nozzle metrics are calculated in two orthogonal, axial spanning planes to determine the impact of the nozzle exit asymmetry, and then they are compared with the circular jet. The shock cell structure, the jet core length, and the axial distribution of the flow at similar radial distances (normalized by the major, minor, or circular radial lengths) are observed to be different between the two planes of the rectangular jet and relative to the circular jet. The dynamics of the large-scale coherent structures differ between the rectangular and the circular jets, in the near-nozzle region, with streamwise vorticity and corner effects being a factor in the rectangular jets, leading to enhanced entrainment. The upstream counter rotating streamwise vortex pairs and their subsequent interaction inhibits axis switching for the rectangular jet cases presented. Overall, far-field noise in the major and minor axis planes is lower than the circular jet for the cold case; however, the noise spectra collapses in the heated case, despite dissimilarities in the near-field flow structures between rectangular and circular jets.

Nomenclature

\mathcal{A}	= aspect ratio
A_e	= exit area
A^*	= throat area
D, D_e	= equivalent diameter
M_j	= design Mach number
u', v', w'	= root-mean-square of the velocity fluctuations

I. Introduction

THE jet noise from high-performance engines for both civilian and military aircraft is an area of active concern on many levels: from the perspective of military personnel on carrier decks to residential areas adjacent to airports and military bases. This has led to efforts to regulate noise levels and mitigate adverse health effects experienced by personnel who work in close proximity to jets during takeoff and landing. Much of the work on noise-reduction techniques has focused on axisymmetric nozzles [1]. This has produced a body of experimental data and simulated noise calculation techniques that give a high level of understanding of jet noise generation, as outlined by Tam [2].

Received 30 September 2016; revision received 31 March 2017; accepted for publication 11 April 2017; published online 27 June 2017. This material is declared a work of the U.S. Government and is not subject to copyright protection in the United States. All requests for copying and permission to reprint should be submitted to CCC at www.copyright.com; employ the ISSN 0001-1452 (print) or 1533-385X (online) to initiate your request. See also AIAA Rights and Permissions www.aiaa.org/randp.

*Research Engineer, Laboratories for Computational Physics and Fluid Dynamics; kamalv@lcp.nrl.navy.mil. Member AIAA.

†Research Engineer, Laboratories for Computational Physics and Fluid Dynamics; ryan.johnson@nrl.navy.mil. Member AIAA.

‡Mathematician, Laboratories for Computational Physics and Fluid Dynamics; andrew.corrigan@nrl.navy.mil. Member AIAA.

§Director, Laboratories for Computational Physics and Fluid Dynamics; kailas@lcp.nrl.navy.mil. Fellow AIAA.

¶Graduate Student; morapa@mail.uc.edu. Member AIAA.

**Graduate Student; baierfn@mail.uc.edu. Member AIAA.

††Distinguished Professor; Ephraim. Gutmark@uc.edu. Fellow AIAA.

Rectangular nozzles offer a number of attractive features for the design of aircraft engines. A 1976 paper by Hiley et al. [3] was one of the first publications that enumerated the advantages of rectangular nozzles over circular ones. In their review of an 18-month collaborative study sponsored by the Air Force Flight Dynamics Laboratory, the authors showed benefits that included reduction of drag when combined with proper body integration, ease of design and production due to fewer parts required for thrust vector control, enhanced exhaust mixing that resulted in reduced infrared signals, and overall performance increase for what the authors called “maneuverability missions.”

The first studies investigating rectangular jets for aircraft applications date back to the late 1950s, where a collaboration of experimental and analytical methods were used for studying two-dimensional nozzle behavior (Sato [4]). The first three-dimensional investigation of rectangular jets was performed by Sforza et al. [5], who produced gross properties of rectangular nozzles that were limited to intrusive measurement techniques. It was not until the late 1970s that detailed investigations of moderate-aspect-ratio jets and their performance began. The first thorough experimental investigation that directly studied the differences between rectangular and circular jets was published by R. A. Kantola in 1979 [6]. Kantola’s experiments found that the overall sound power level was 3 dB less for a rectangular jet of high aspect ratio in comparison to a circular jet of equivalent area. Kantola attributed these differences to mean flow, or “shielding,” characteristics. Additionally, this publication demonstrated that the largest difference occurred in the high-frequency domains of the sound pressure level (SPL) and that the rectangular jet’s minor axis plane was louder than the major axis plane.

Following Kantola’s initial study [6], research studies examined rectangular jet mixing of both subsonic (Krothapalli et al. [7], Husain and Hussain [8], and Grinstein [9]) and supersonic rectangular jets, with the focus on turbulent mixing, axis switching, and flow similarity (Gutmark et al. [10], Kim and Samimy [11], and Zaman [12]). For a comprehensive review of rectangular jet flow experiments, we refer the reader to the work of Gutmark and Grinstein [13]. For early works following Kantola [6] that focused on noise, we refer the reader to the work of Krothapalli [14], Raman and

Rice [15], and Kolbe et al. [16]. To this day, experimental investigations have generated a great body of work that continued to explore the different elements of rectangular jet noise [17–21]. However, very few investigations have detailed flowfield statistics and mapping of the large-scale coherent structures in the near field along with the resultant far-field acoustics.

The nozzles modeled in the present paper are a low-aspect-ratio ($\mathcal{R} = 2.0$) rectangular nozzle with converging–diverging (CD) walls in the minor axis plane and parallel walls in the major axis plane, along with a circular nozzle having the same equivalent diameter and area ratio. The asymmetry of the rectangular nozzle is investigated within the context of how it affects the far-field noise and the jet flow characteristics that might be a potential modulating parameter that can directly affect far-field noise. The contrast with axisymmetric flow is obtained by comparing with an equivalent circular nozzle. The nozzle geometries, presented by Heeb et al. [21], are covered in detail in Sec. II. Simulations were performed using Laboratories for Computational Physics and Fluid Dynamics's jet engine noise-reduction code (known as JENRE). The computational methodology and procedure are covered in Secs. III and IV, respectively. We validated the rectangular and circular jet simulations in this work by comparing the computed far-field noise data to the data recorded by experiments at the University of Cincinnati [22], and we present these comparisons in Sec. V. We then directly compare our rectangular jet results for two nozzle temperature ratios to simulations of the circular jet for the same operating conditions. This comparison and analysis are covered in Sec. VI.

II. Nozzle Geometry and Operating Conditions

Figure 1 shows the cross-sectional views of the rectangular and circular nozzle geometries. The rectangular nozzle used in this study is the same biconic converging–diverging nozzle from the University of Cincinnati as reported in [21]. The rectangular exit has an aspect ratio \mathcal{R} of two with an equivalent exit diameter D_e of 0.02065 m. The nozzle's area ratio (A_e/A^*) is 1.18 with a design Mach number M_j of 1.5, which corresponds to a nozzle pressure ratio (NPR) of 3.67. The nozzle is sharply convergent–divergent in the cross-sectional minor axis plane. The wall profile starting from the inlet converges as a sudden linear decline to the throat plane and then linearly diverges to a rectangular exit plane of dimensions 0.0259×0.01295 m. In the plane parallel to the major axis, the nozzle walls have a straight profile

from the inlet to the nozzle exit. The circular nozzle geometry has the same equivalent diameter and design Mach number as the rectangular nozzle with a sharply convergent–divergent throat section.

Simulations are done for the ideally expanded case (NPR of 3.67) for two nozzle temperature ratios ($TR = T_o/T_{atm}$) of one and three for both geometries. This provides data for comparison between the asymmetric and axisymmetric geometries for cold and heated jets. The ambient conditions are $P_{atm} = 101.325$ kN/m² and $T_{atm} = 300$ K. The characteristic velocity and length scales used for normalization are the ideally expanded exit velocity U_j and the equivalent diameter D_e . The equivalent diameter is defined as the diameter of a circular jet having the same exit cross-sectional area. For convenience, D is used interchangeably with the equivalent diameter D_e through the rest of the text because only one such parameter exists. For the cold jets, this gives a typical $Re = U_j D_e / \nu \approx 551,000$; for the heated jets, it is $Re \approx 150,500$ with the air viscosity based on dry air tables.

III. Computational Methodology in JENRE

Simulations were performed using the jet noise-reduction (JENRE) code developed at the U.S. Naval Research Laboratory [23,24]. JENRE provides unsteady compressible flow solver capabilities that support various numerics (cell-centered finite volume or nodal finite element method) while delivering high throughput on calculations. It was developed with an emphasis on raw performance and the ability to exploit emerging massively parallel high-performance computing (HPC) architectures. It supports different HPC parallel programming paradigms for message passing (such as MPI, OpenMP, CUDA) and hybrid models, depending on the HPC cluster architecture. A key bottleneck of HPC throughput is data input–output (IO). JENRE supports parallel IO via MPI/IO or the adaptable IO system to further complement the multiple levels of parallelism.

JENRE was used in this work to solve the compressible Euler equations:

$$\frac{\partial \rho}{\partial t} + \nabla \cdot (\rho \mathbf{v}) = 0 \quad (1)$$

$$\frac{\partial \rho \mathbf{v}}{\partial t} + \nabla \cdot (\rho \mathbf{v} \otimes \mathbf{v}) = -\nabla p \quad (2)$$

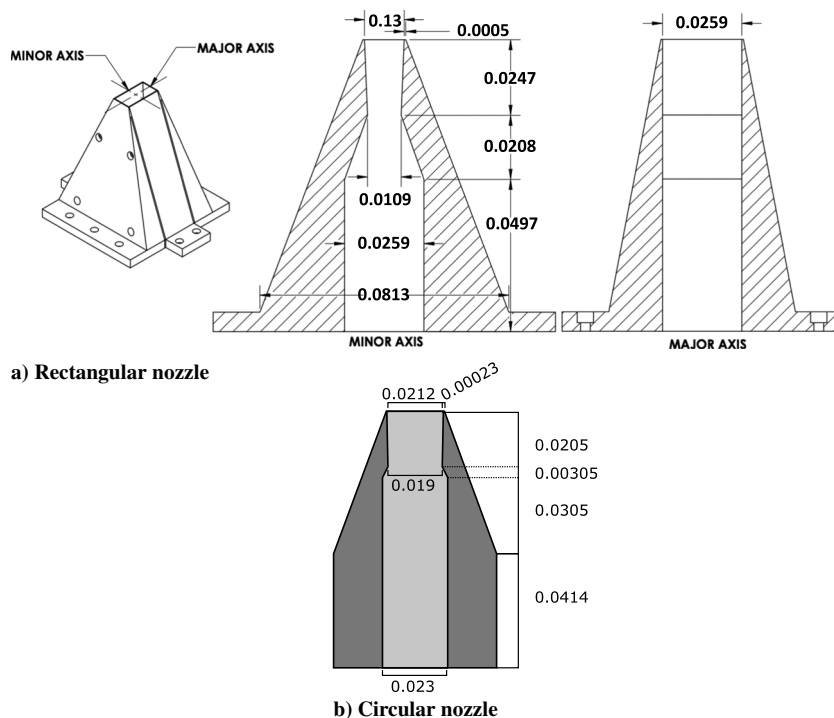
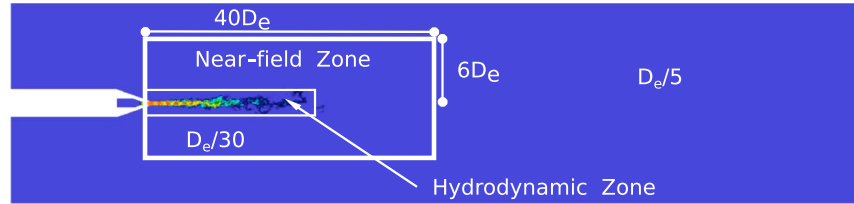
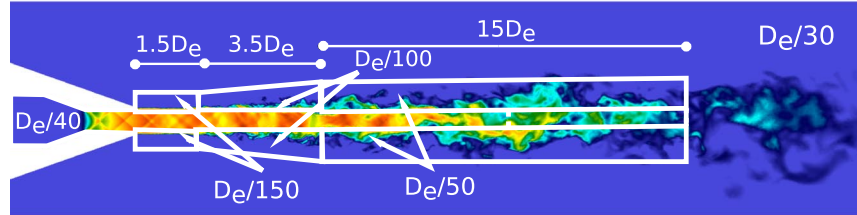


Fig. 1 Nozzle geometry cross-sectional views. All units in meters [21].



a) View of the simulated domain's minor plane



b) Near-field zone details

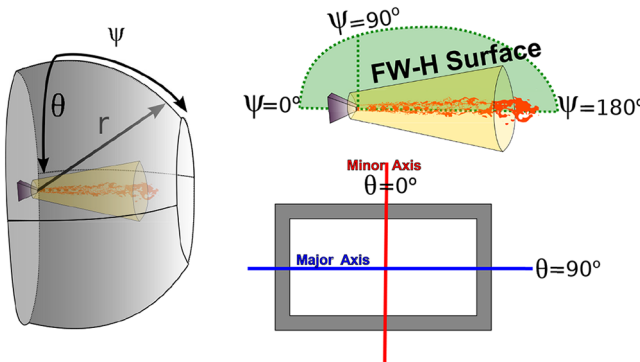
Fig. 2 Computational domain boundaries.

$$\frac{\partial \rho E}{\partial t} + \nabla \cdot (\rho(E - p/\rho)\mathbf{v}) = 0 \quad (3)$$

with the ideal gas law for closure: $p = (\gamma - 1)u$. Here, ρ is density, \mathbf{v} is the velocity vector, p is pressure, E is the specific total energy, γ is the ratio of specific heats, and u is the specific internal energy. Equations (1–3) are solved in JENRE using an edge-based

formulation for all flux integration and limiting algorithms [25]. The Taylor–Galerkin finite element method with second-order spatial accuracy, for tetrahedral cells, is used for the current cases along with the finite element flux corrected transport (FCT) [26–29] method. The multidimensional FCT flux limiter provides an implicit subgrid stress model, which ensures monotonicity at shocks and sharp gradients with minimal artificial dissipation.

Specific to jet noise processing, JENRE supports in situ calculation of far-field noise data using the Ffowcs-Williams and Hawking (FW-H) [30] approach, using resolved near-field data in the domain. This greatly decreases noise-processing-related IO and storage; and it outputs the overall SPL (OASPL), the SPL, and the spectrum of the normalized pressure fluctuation as a spectral density field for specified locations at the far field. For the current simulations, far-field data are gathered at a sweep of polar array of locations from 35 deg upstream to 170 deg downstream, at a distance of $40D_e$, that sweeps around the nozzle about the jet centerline. With such a span of recording locations, we can investigate the asymmetric nature of the rectangular jet noise generation and record observer orientation dependence of the noise propagation for the current setup.



a) Illustration of far field b) Illustration of near field
Fig. 3 Illustration of far field, near field, Ffowcs-Williams and Hawking surface, minor and major axes, and θ and ψ locations.

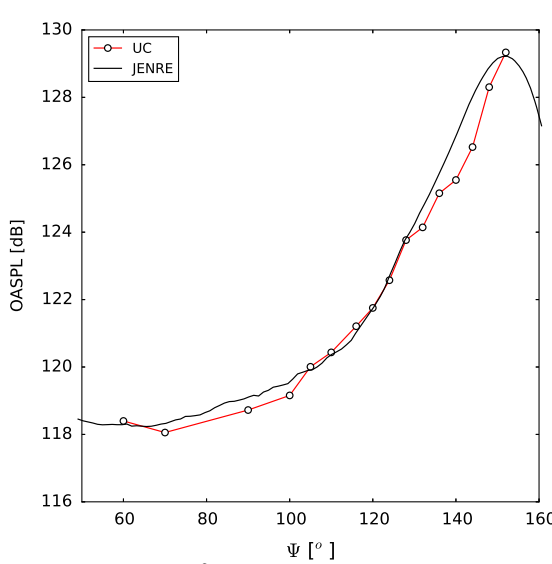
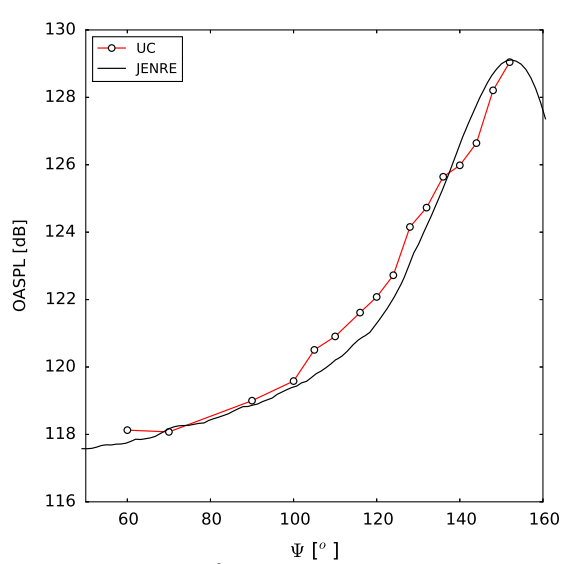
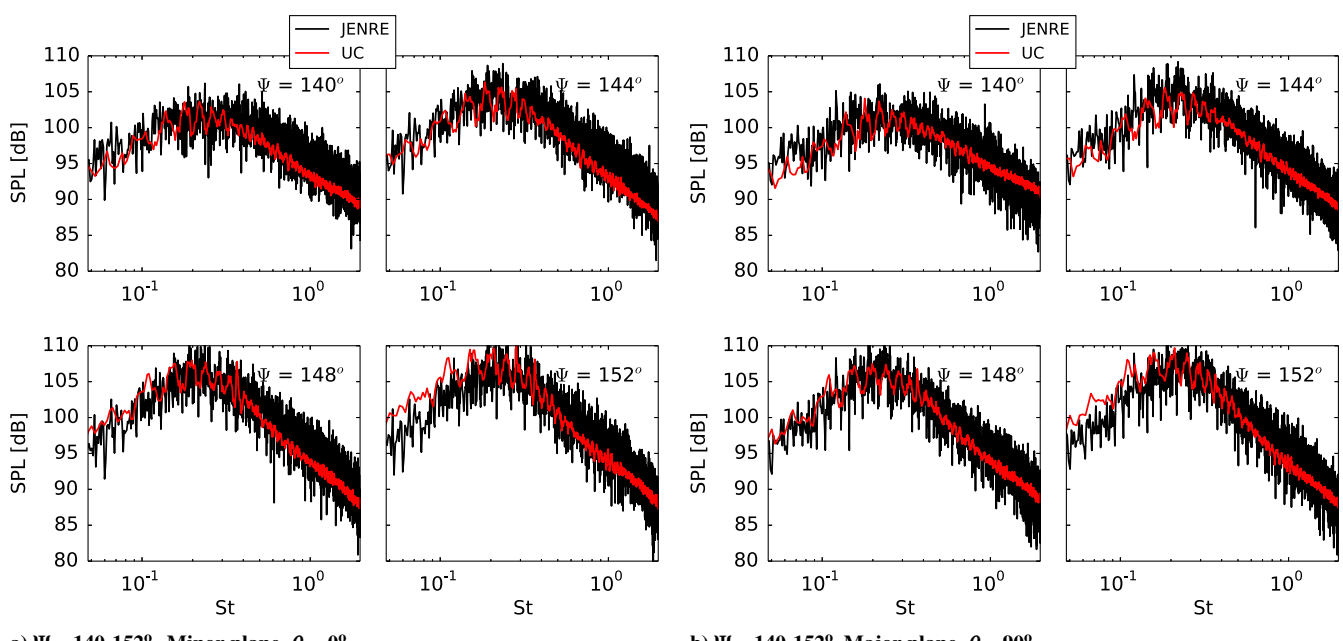
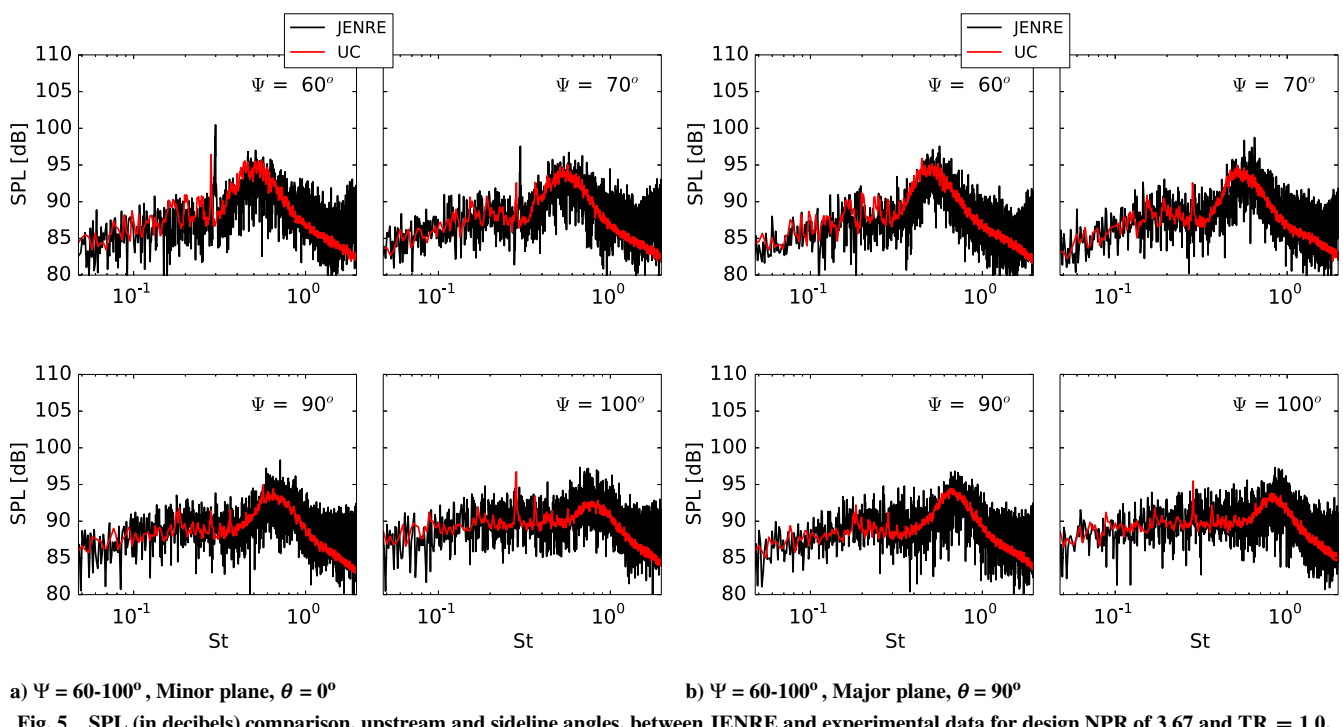
a) Minor plane, $\theta = 0^\circ$ b) Major plane, $\theta = 90^\circ$

Fig. 4 OASPL (in decibels) comparison: design NPR = 3.67, and TR = 1 (UC, University of Cincinnati).

accurate and validated results for a circular nozzle geometry with overall sound pressure levels agreeing within 1 dB. The outline of the computational domain and the grid spacing within are shown in Fig. 2 as a plane cut through the minor axis. For clarity, the details for this mesh in Fig. 2 are overlaid on an instantaneous solution for the Mach number. The computational domain extends $10D_e$ upstream of the nozzle exit and $100D_e$ downstream. The grid extends radially $15D_e$ from the both the major and minor axis planes, which results in a rectangular exterior. The entire domain has a base grid spacing of $D_e/5$, with appropriate refinement zones in the volume surrounding the nozzle exit to capture the near-nozzle shocks, the shear-layer flow structures, and the near-field region. This inner volume, shown as the outermost white rectangle and labeled as the near-field zone in Fig. 2a, extends $40D_e$ in the axial direction with a $12D_e \times 12D_e$ rectangular cross section. It has a maximum grid spacing of $D_e/30$

that is sufficient for the FW-H surfaces extracted from the simulations within this volume for near-field noise source data. There are multiple refinement zones within this region that correspond to Liu et al.'s [31] refinement choices. From the nozzle exit, for a distance of $5D_e$ downstream, the spacing is a maximum of $D_e/150$ for better mixing layer resolution. This transitions to a larger zone with grid spacing of $D_e/50$ extending $15D_e$ downstream for the turbulent mixing noise. The entire nozzle geometry and the core flow, to a distance of $20D_e$, have a grid spacing of $D_e/40$. Radially, past the shear layers, the grid density relaxes gradually, falling to a maximum spacing of $D_e/30$ around $10D_e$. Beyond the dense region, the grid coarsens out all the way to the boundary. A numerical sponge layer is defined very close to the domain boundaries to dampen out any reflections from the boundary from propagating inside. The grids generated were on the order of 35 million nodes using these grid specifications.



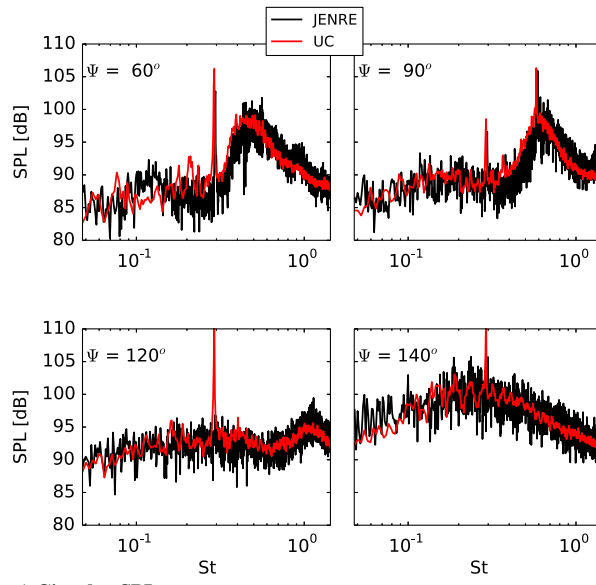
The nozzle inlet has stagnation pressure and stagnation temperature boundary conditions prescribed to match the operating conditions for the ideally expanded NPR with two different nozzle temperature ratios. The nozzle walls are modeled using a slip boundary condition. The outer domain boundary is set to the ambient flow using characteristic boundary conditions. A buffer zone is implemented near the far-field boundaries to remove any wave reflections.

V. Validation of JENRE

Figure 3 illustrates the designation of the minor and major axes and their corresponding θ values, as well as the values of ψ upstream and downstream within a plane. For the circular jet, the data were recorded at $\theta = 0$ deg with other parameters the same.

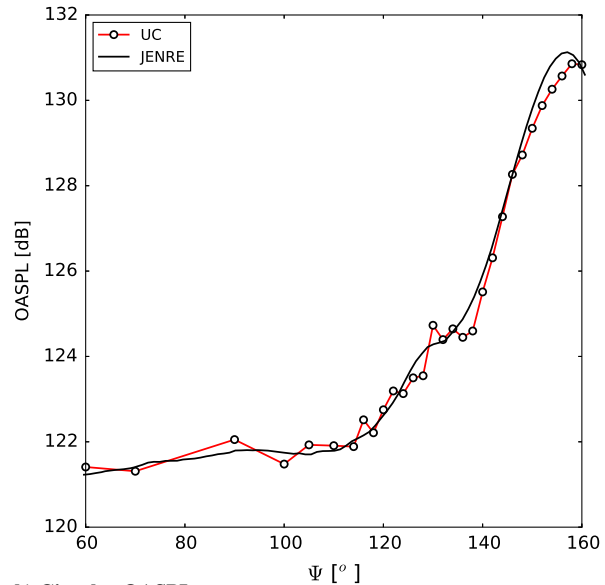
Within the JENRE simulations, near-field data were collected on a FW-H surface and projected to the far-field locations; the near-field FW-H surface is illustrated by the conical frustum enclosing the jet plume shown in both Figs. 3a and 3b. The specific FW-H surface used

for this validation work has an inner radius of $2.5D_e$ at an axial location of $0.5D_e$ behind the nozzle exit plane and extends to $27D_e$ in the axial direction with a downstream radius of $5D_e$. These distances were chosen by the procedure described by Liu et al. [31]. Different conical frustums of the FW-H surface, still within the near-field zone in Fig. 2 and outside of the hydrodynamic pressure fluctuations, resulted in negligible differences in sound data: less than 0.1 dB in OASPL. Large-eddy simulation data were recorded and sampled on the FW-H surface for a total time of $600 D_e/U_j$ at a rate of 80 KHz with 4096 bins. The Strouhal number St for plotting the sound spectra was defined as $f * D_e/U_j$, where f was the frequency. Experimental data from the University of Cincinnati, for the ideally expanded cases and for both geometries, were used for JENRE validation. Using sound pressure level data, with a frequency resolution of 50 Hz and an overall sound pressure level in chosen planes at specified locations, the far-field noise calculations were compared with experiments for the combinations of the operating conditions listed previously. For the rectangular nozzle geometry, experimental data were recorded in the minor axis plane ($\theta = 0$ deg) and the major axis

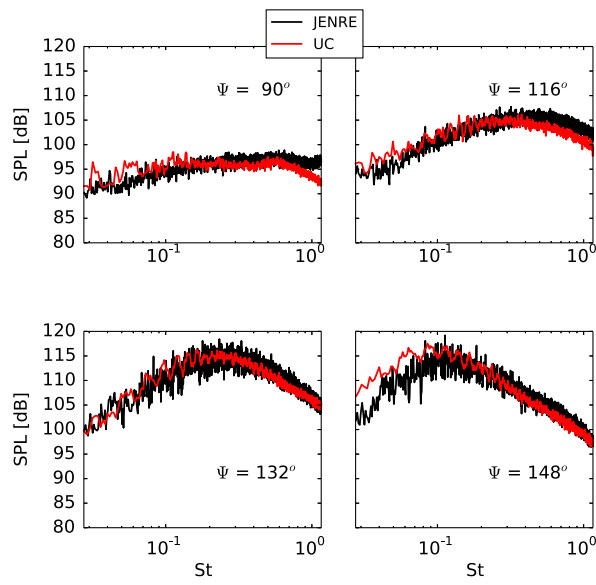


a) Circular SPL

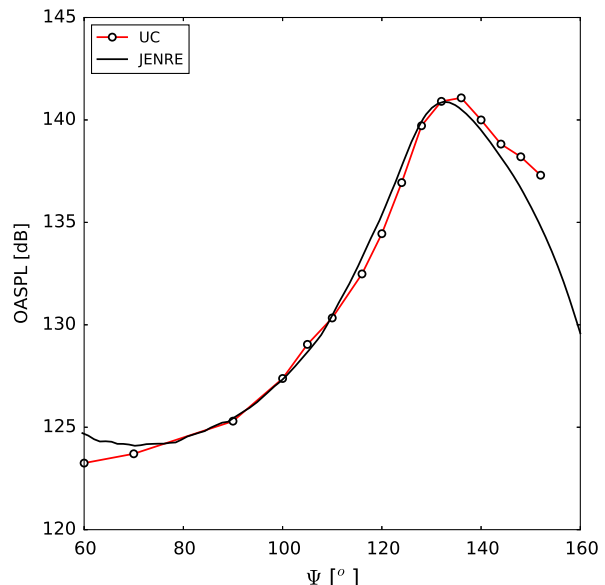
Fig. 7 OASPL (in decibels) and SPL (in decibels) comparison with experimental data, with design NPR of 3.67 and TR = 1.0.



b) Circular OASPL

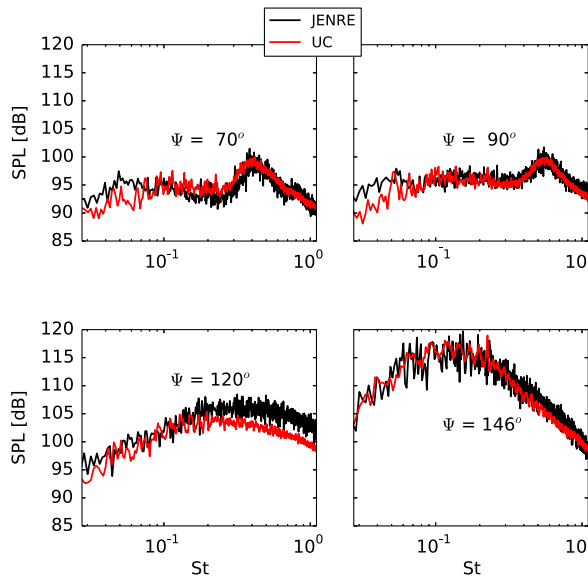


a) $\Psi = 90\text{--}148^\circ$, Major plane, $\theta = 90^\circ$

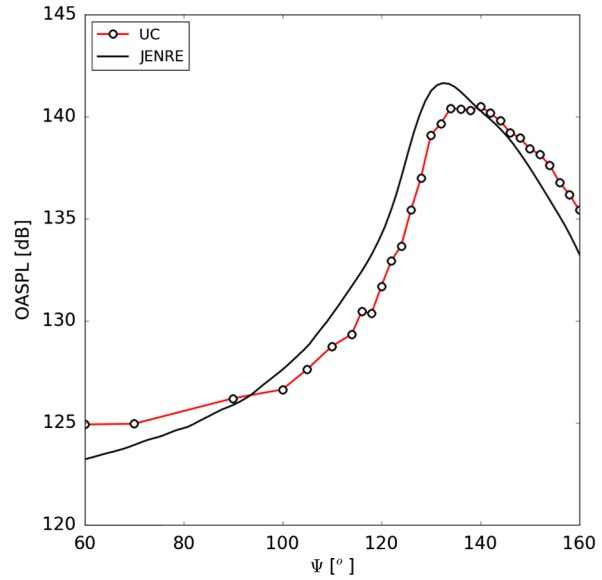


b) Major plane, $\theta = 90^\circ$

Fig. 8 OASPL (in decibels with reference pressure of $20 \mu\text{Pa}$) and SPL (in decibels) comparison with experimental data. Design NPR = 3.67, TR = 3.0.



a) Circular SPL



b) Circular OASPL

Fig. 9 OASPL (in decibels) with regard to and SPL (in decibels) comparison with experimental data, with design NPR of 3.67 and TR = 3.0.

plane ($\theta = 90$ deg) at a far-field distance of $40D_e$, from $\Psi = 60$ to 160 deg, at 16 different polar arrays of microphone locations.

Figure 4 shows the computed and measured OASPL results for different polar angles Ψ in both the minor axis plane (Fig. 4a) and the major axis plane (Fig. 4b). The simulated OASPL numbers and the curve profile across the elevation angles compare well, to within 1 dB, with the experimentally recorded values.

Figures 5 and 6 show the sound pressure levels for polar angles Ψ ranging from 60 to 152 deg for the cold rectangular jet for both major and minor axis planes with experimental data. At the upstream and sideline locations, the high-frequency broadband peaks, associated with shock noise, are captured well. At the downstream locations, the low-frequency peak, associated with the flowfield structures, overlaps with the experimental data. The overall SPL distribution trend and magnitude at each location have very good agreement, and this is reflected in the matching peak noise radiation direction in the OASPL results in Fig. 4. These results validate JENRE's capability to resolve noise sources across the sound pressure level spectrum and specific tones found in experimental setups. For example, the screech tone at approximately 5500 Hz present in the experimental data at upstream angles of $\Psi = 60$ and 70 deg has a matching tone in the JENRE calculations.

Validation for the cold circular jet is shown in Fig. 7. Figure 7a shows the capture of the broadband peaks at upstream and sideline locations and the low-frequency peak at the downstream location. This gives good agreement with the experimental data for the OASPL values at all elevation angles, including the noise peak radiation direction, with the overall comparisons being within 1 dB, as seen in Fig. 7b. The heated jet validations for the rectangular and circular jets are shown in Figs. 8 and 9 with similar results.

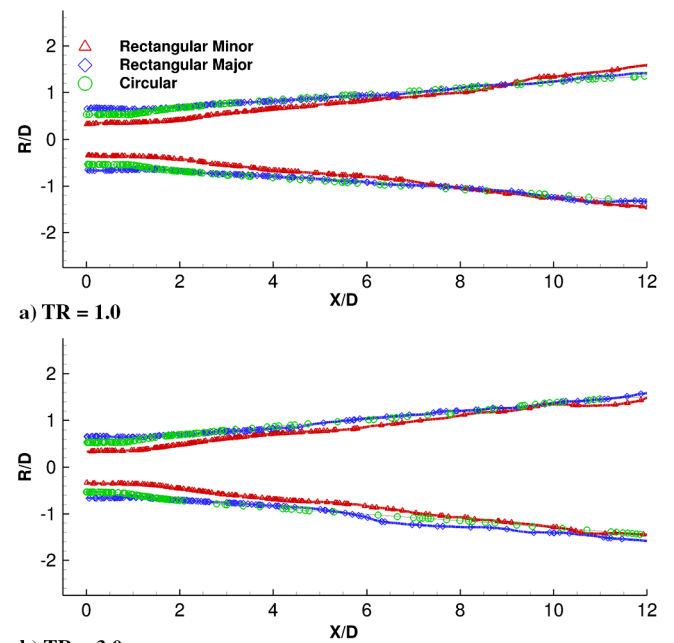
VI. Analysis

A. Jet Plume Spread

With an asymmetric geometry such as the rectangular nozzle, there is asymmetry in the jet flow due to the combination of the nozzle walls' sharp corners and the different distances of the major and minor axis walls from the axial core. Differences in the flow spreading rate between major and minor planes in the near field of the rectangular jet and further downstream have been investigated by Gutmark et al. [10]. Axis switching [32] is a phenomena that results from such interactions when the spreading of the flow in the minor axis plane surpasses the major axis plane; at a point downstream, there is a crossover when the asymmetry inverts and the major axis becomes the minor, and vice versa. Figures 10a and 10b show the

time-averaged jet plume spread, using $M = 0.2$ contours, for the cold and heated jets. X/D and R/D are the nondimensional axial and radial distances. It is seen that, near the nozzle exit, the plume spreading rates are different between the minor axis and major axis planes, and asymmetry is present in the flow for each temperature case. As the flow develops, they converge at a point downstream; past that, there is no discernible difference between the plume spread in each plane. Any sustained plume asymmetry for this rectangular nozzle geometry with an aspect ratio of two, at the design condition for both cold and heated jets, is absent, and no axis switching is observed.

Comparing Figs. 10a and 10b, the plume spread in each plane differs between the cold and the heated rectangular jets. For the cold jet, as seen in Fig. 10a, the major and minor axis plane plumes start spreading sharply past $X/D = 2$. For the heated jet, however, the spread happens earlier past $X/D = 1$. Increasing the jet temperature increases the initial shear-layer growth rate, leading to enhanced mixing.

Fig. 10 Axial spread of the supersonic rectangular jet shown using $M = 0.2$ contours: a) cold jet and b) heated jet.

The circular jet plume spread aligns mainly with the rectangular major axis plane plume spread for both temperature cases. However, there are some differences close to the nozzle exit. The circular plume starts spreading closer to the nozzle than both rectangular plumes in the case of the cold jet (Fig. 10a); whereas for the heated case, they are almost similar, with the spread starting early. Past the initial region near the nozzle exit (approximately $3D$), the plume spreading rates for both geometries are similar at a given temperature ratio. Hence, the impact of the asymmetric geometry does not result in sustained asymmetric plume spread downstream for the operating conditions and geometry simulated.

B. Near-Field Shock Cell Structure

Figure 11 shows the time-averaged streamwise velocity distributions in the major axis and minor axis planes for the rectangular jet and in the center plane for the circular jet. For the cold and heated jets, the double-diamond shock cells at the nozzle exit, from the throat shock and the lip shock, are visible in the minor axis plane and the center plane. The throat shock originates from the sharply convergent-divergent profile in the throat section for the circular nozzle and the minor axis plane of the rectangular nozzle. The major axis plane of the rectangular nozzle has straight walls; hence, only the lip shock is seen that interacts with the smaller shock

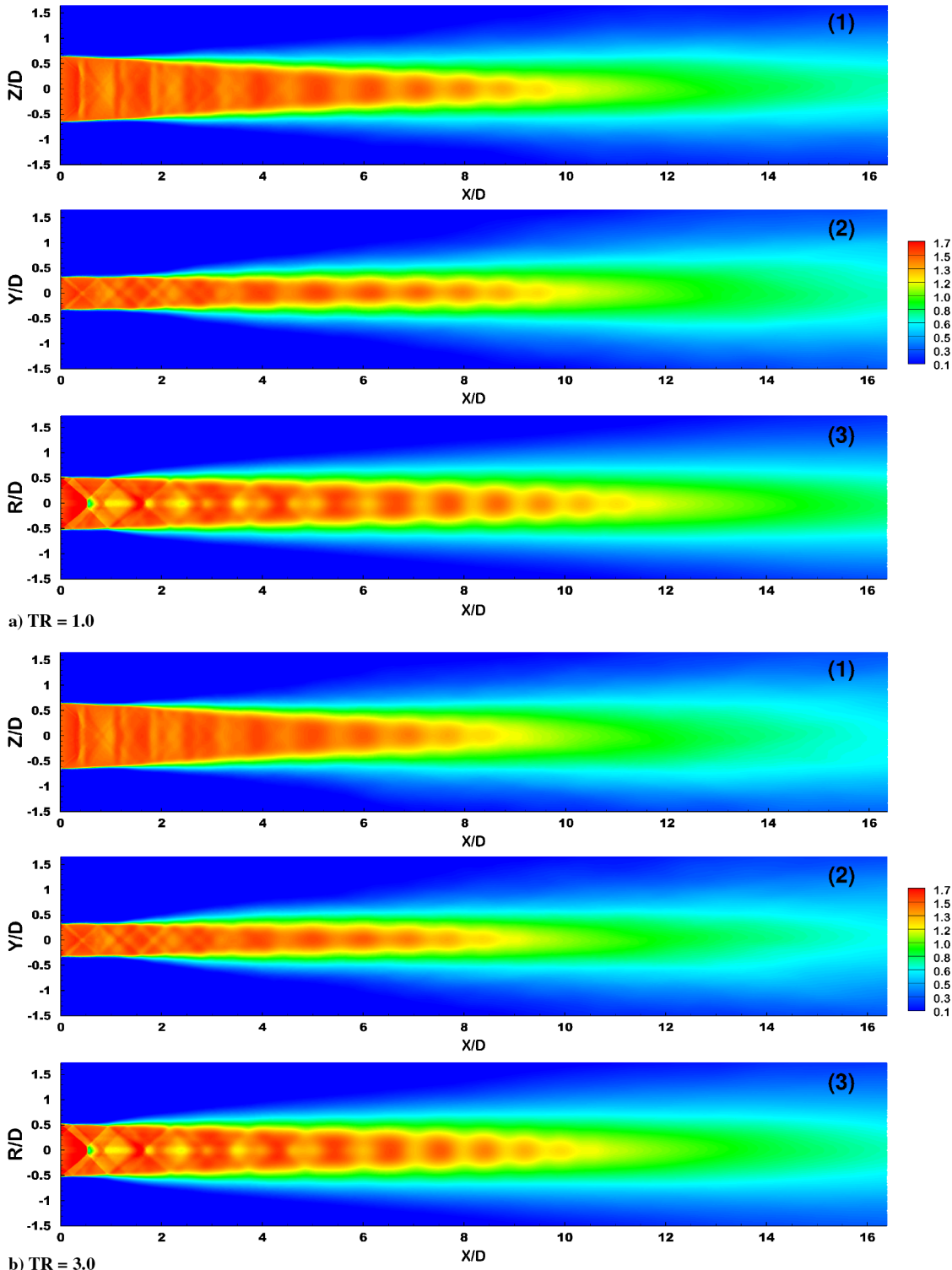


Fig. 11 Time-averaged velocity distributions for the cold and heated jets: major axis plane (denoted by 1), minor axis plane (denoted by 2), and center plane from circular jet (denoted by 3).

cells in the minor axis plane. There is a Mach disk impacted region near the centerline axis for the circular jet. The near-field shock cell locations, size, and strength are different across all three planes for the

cold jets. The heated cases show the same differences in the near field with earlier decay of the shock cells in the streamwise direction. The enhanced mixing in the heated jets also significantly shortens the jet

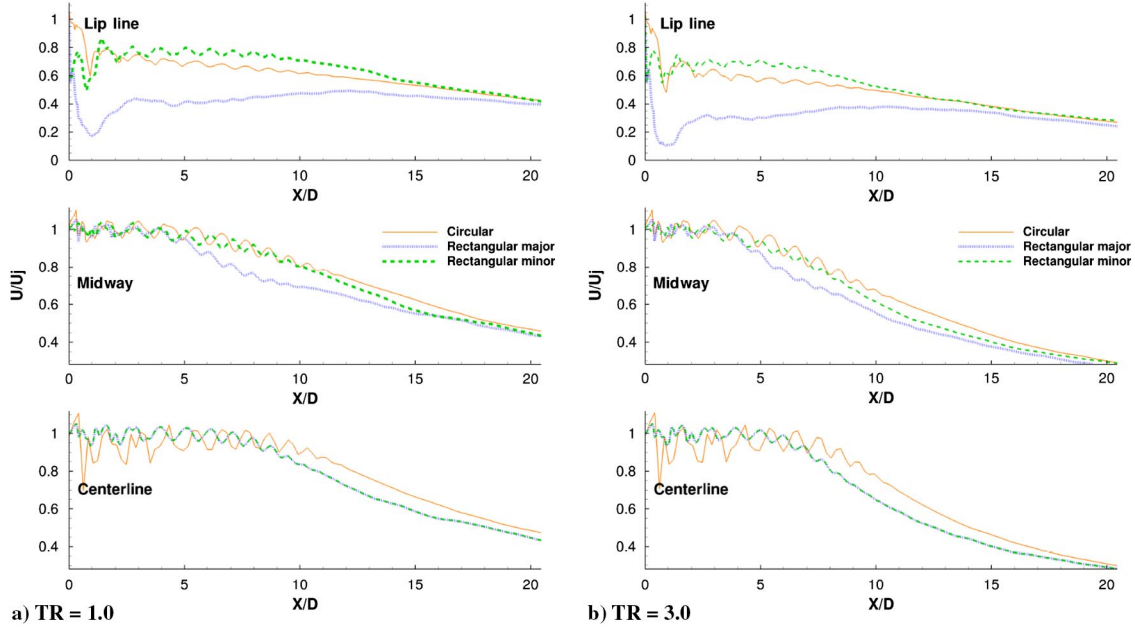


Fig. 12 Axial velocity distributions at the centerline, lip line, and midway line between the two axial locations: a) cold jet and b) heated jet.

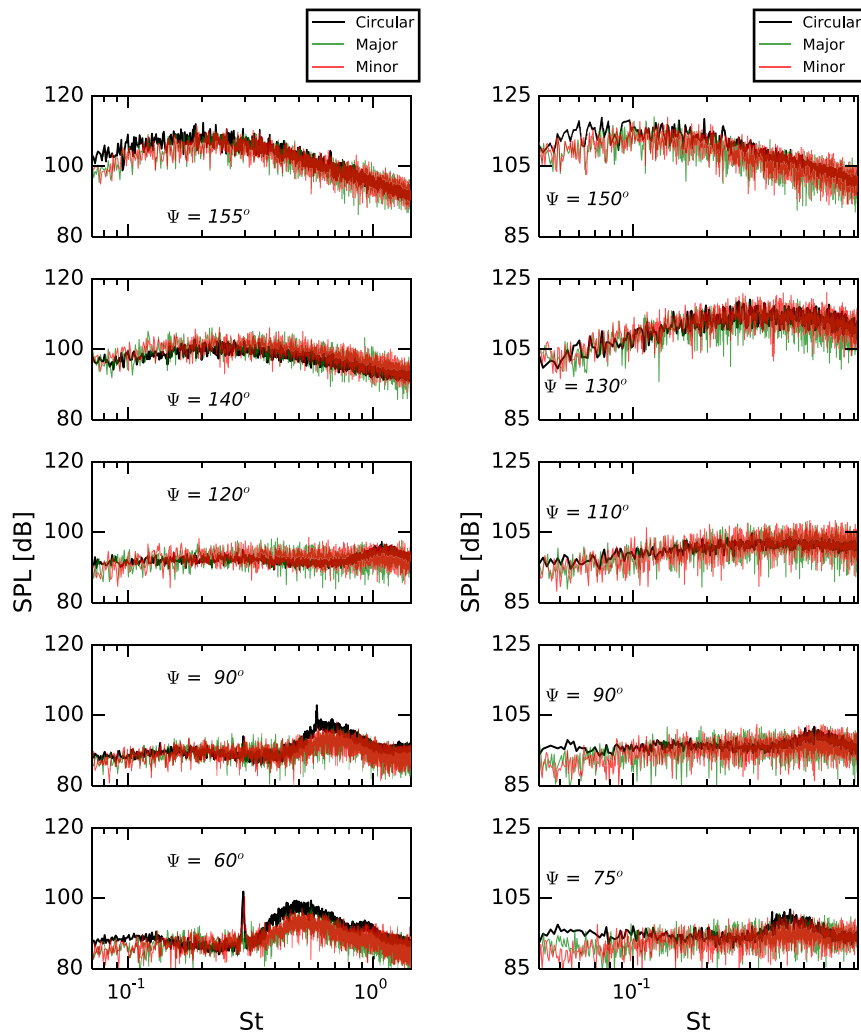


Fig. 13 SPL for circular and rectangular jets. Major and minor axis results are shown with transparency to show overlay of data.

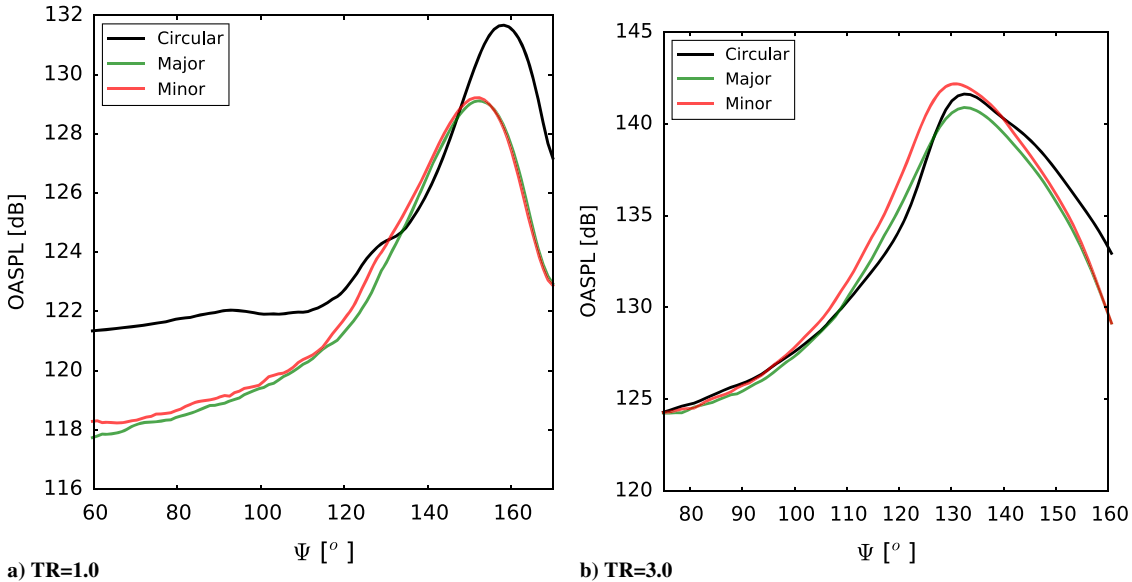


Fig. 14 OASPL (in decibels) for major and minor locations, calculated from S_θ , with circular results for comparison.

core lengths, defined as the location where the streamwise velocity reaches $0.95U_j$ on the centerline.

Figure 12 shows the time-averaged axial velocity distributions of both the cold and heated jets at three radial locations in each plane: the centerline, the lip line, and the midway point between the two. The centerline distributions, from Fig. 12b, confirm the shorter jet core length for the heated jets. The rectangular cold jet core length is approximately $8.1D$, and it is $9.6D$ for the circular jet. In the heated case, the respective values are $6.2D$ and $7.7D$, respectively, which gives a difference of $2D$ for both cases. The heating of the jet has a low impact on the shock cell attributes, as is evident from these line cuts, with the profiles being similar between the nozzle exit ($0D$) and $5D$ for both the cold and heated cases. The velocity distributions of the circular jet are closer to the minor axis plane profiles, for both temperatures. The lip-line axial distributions have the largest variation, with the minor axis plane velocities being much higher than the major axis plane velocities. The minor lip line initially has two peaks due to the double-diamond shock cell at the nozzle exit. The lip line in the minor plane continues to register small peaks downstream due to the impact of the shock cell reflections on the shear layer. The lip line of the circular jet exhibits a profile similar to the minor axis plane. Both the minor and the circular jet lip lines start decaying past the jet core length distance for both the heated and cold jets. The major axis plane lip line holds relatively steady downstream until it converges with the minor plane lip line past $20D$.

Figures 11 and 12 demonstrate that, for a given temperature ratio, the shock cell structures and the time-averaged streamwise velocity distributions along geometrically similar axial lines in each plane (midline and lip line) differ between the major, minor, and circular jet planes. However, increasing the operating temperature does not impact the shock cells, other than hastening the decay in each plane.

C. Noise Production

In this section, we examine the difference in the far-field noise between the rectangular and circular jets with the same design

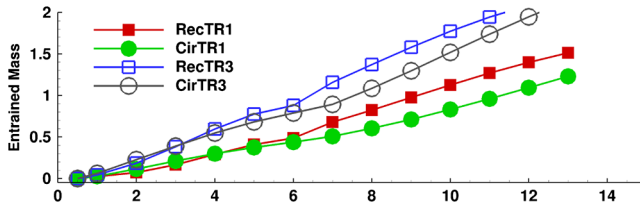


Fig. 15 Mass entrainment (RecTR1, rectangular nozzle, $TR = 1.0$; RecTR3, rectangular nozzle, $TR = 3.0$).

condition Mach number and equivalent diameter. The noise metrics are compared in the minor ($\theta = 0$ deg) and the major ($\theta = 90$ deg) axis planes, as well as in the circular jet at $\theta = 0$ deg (see Fig. 3b). For the axisymmetric circular jet, the chosen theta is a representative plane with the noise at a given elevation location being an average of all power spectral density samples [$S(\Psi, f)$] at all θ locations:

$$S(\Psi, f) = \frac{\sum_{n=1}^{N_s} \sum_{k=1}^{N_\theta} S_{k,n}(\Psi, f)}{N_s N_\theta} \quad (4)$$

Here, k is the index of the θ location, and n is the index of a sample. For example, $S_{1,4}$ is the power spectral density data found from the fourth sample at the first theta location of $\theta = 0$ deg. For the cases presented here, we have 20 circumferential spatial θ locations and record data at those locations for eight time samples. This results in $N_s = 8$ and $N_\theta = 20$, for a total of 160 samples. For the asymmetric rectangular jet, spatial azimuthal θ averaging cannot be used. For azimuthal location-dependent data, an average of the power spectral density at the specific location is taken:

$$S_\theta(\Psi, f) = \frac{\sum_{n=1}^{N_s} S_{\theta,n}(\Psi, f)}{N_s} \quad (5)$$

For S_θ to reach the same number of samples as S , the simulations would each need to run 20 times as long, which is computationally prohibitive. For this study, we found that eight samples were sufficient for an accurate planar SPL with a frequency resolution of 50 Hz and OASPL prediction; see Sec. V. However, the lower number of samples resulted in an increased excursion of the oscillations and a wider SPL band of the recorded spectra.

Figure 13 shows the SPL calculated from the aforementioned averaged power spectral densities for the rectangular and circular jets. Each column is a fixed temperature ratio. For the cold jet, as seen in Fig. 13a, the SPL for the major and minor axis planes of the rectangular jet practically overlap, whereas the circular jet has a significant deviation. At the upstream ($\Psi < 90$ deg) and sideline ($\Psi = 90$ deg) locations, the broadband noise peak magnitude differs, as well as the overall noise level, with the circular jet having a higher SPL noise profile. There are discrete tones present in the circular jet spectrum; for the upstream observer location ($\Psi = 60$ deg), a similar tone is present in the minor axis plane spectra. At these locations, the primary contribution to the broadband noise spectra comes from the shock-associated noise and, as described in Sec. VI.B, the shock cell structure is different between the circular and rectangular jets. At the downstream locations, the low-frequency mixing noise dominates the spectra. At $\Psi = 140$ deg, the circular and rectangular jets' SPL

profiles are close but, farther downstream, the low-frequency spectra deviate by more than 5 dB at $\Psi = 155$ deg.

When the operating temperature is raised, the mixing noise increases the overall noise level (Fig. 13b) and the shock-associated noise component contributes less to the overall noise because the shock cell structures near the nozzle exit do not show a strong dependence on the temperature. At the upstream and sideline locations, the circular jet SPL profile does not deviate significantly from the rectangular jet profiles, especially in the broadband peak spectra. For the downstream locations, the circular and rectangular major and minor axis plane SPLs overlap until the circular SPL starts deviating further downstream, as seen at $\Psi = 150$ deg. The mixing noise is dominating the spectra in all planes, and the circular and rectangular jet SPL profiles are clustered more closely than the cold jet case.

Figure 14 shows the OASPL in the minor and major axis planes of the rectangular jet compared with the circular jet. Consistent with the SPL noise profiles in the cold jet cases, the circular jet OASPL curve is very different from the overlapping OASPL curves of the minor and major axis planes. Differences of up to 3.5 dB occur at the upstream and sideline locations and in the peak noise propagation direction of $\Psi = 155$ deg. For the heated jet cases, the SPL profile differences are minimal, and all the OASPL curves lie within 2 dB of each other, with no significant difference between the circular and

rectangular jets. Additionally, the peak noise radiation direction shifts upstream ($\Psi \approx 130$ deg) in the heated cases, which is consistent with Liu et al.'s findings [31].

D. Mass Entrainment, Vorticity, and Turbulence Intensities

1. Mass Entrainment

A significant difference between the circular and rectangular jets is the impact of the nozzles' corners on the evolution of the cross-sectional shape of the jet. It has been shown [7,11,12,33–35] that they offer a passive way of improving mixing for low-aspect-ratio jets through both large-scale entrainment due to coherent structures and fine-scale mixing at the corners. Streamwise vortices are considered to be one of the main components that play a dominant role in enhancing the mixing for asymmetric nozzles [11,12,33]. The streamwise vorticity ω_x is derived from the variation of the self-induction of the azimuthal vortex around the nozzle lip curvature: ω_θ -dynamics. This was observed in jets, vortex generators, and when forced excitation was applied to these flows. In the current low-aspect-ratio rectangular jet, the azimuthal vortex ring deforms as it convects downstream, with the minor plane ring section stretching streamwise faster than the major plane section. The significant self-induction at the sharp corners sets up a different dynamic for the way the rings stretch at the corners.

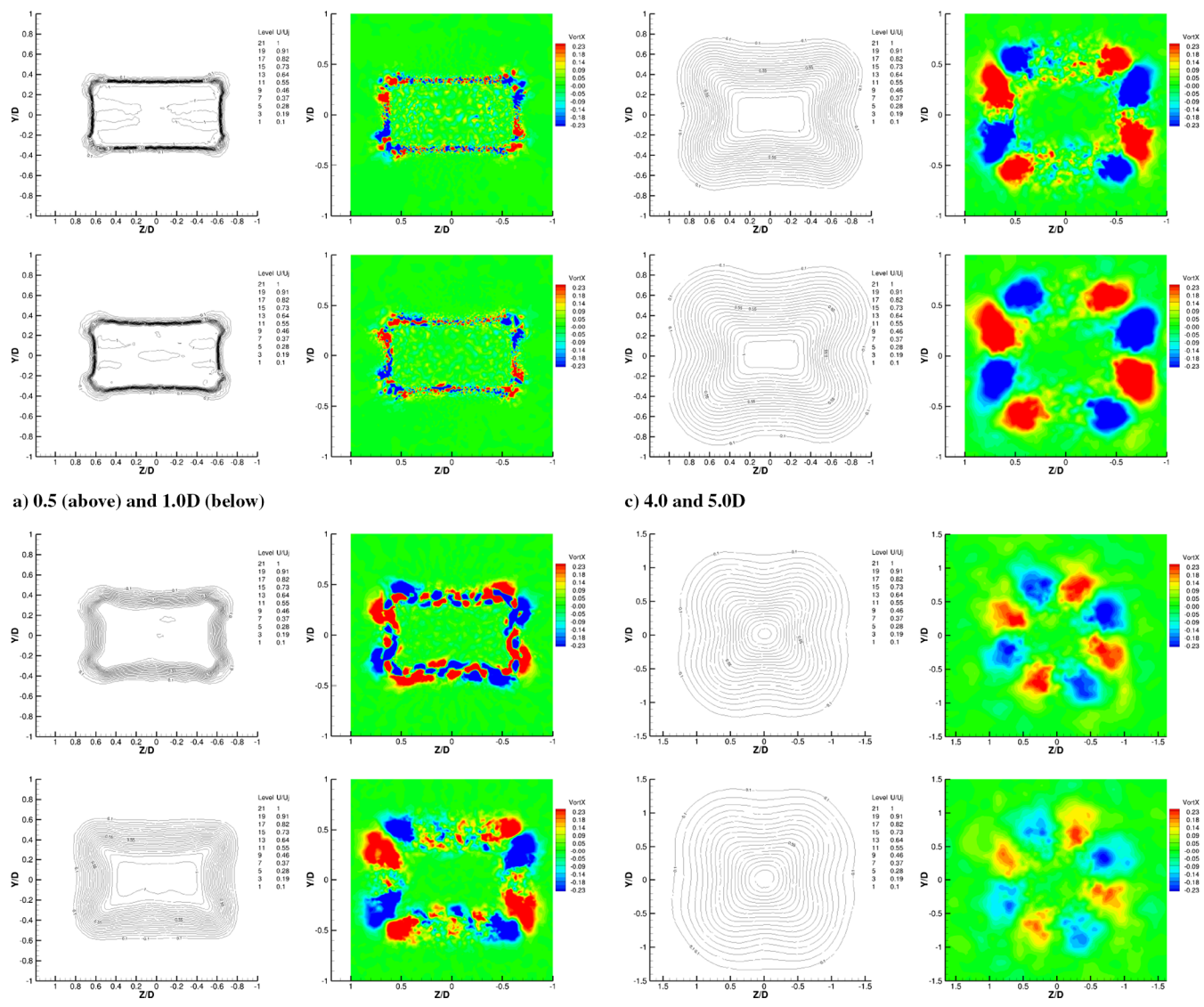
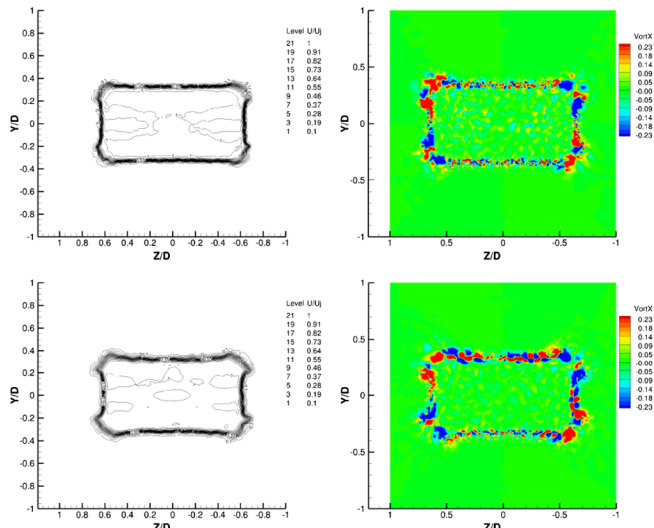


Fig. 16 Time-averaged velocity contours and axial vorticity for TR of 1.0. Plotted area changes are between 5.0D and 8.0D.

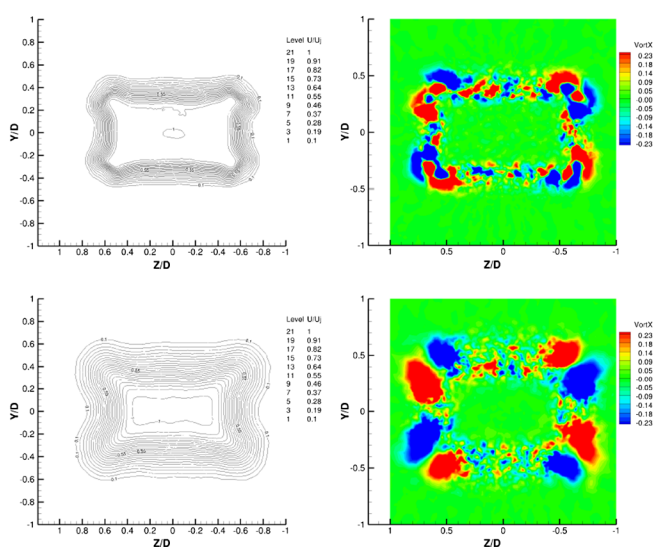
Figure 15 shows the time-averaged mass entrainment at subsequent cross sections in the streamwise direction. The mass flow is defined as follows:

$$(q - q_{0.5D})/q_{0.5D}$$

where q is the integral of the mass flux across the cross-sectional plane perpendicular to the jet centerline. The trends show higher mass entrainment for the rectangular jet when compared to the circular jet for cold and heated jets. This is in line with what has been observed experimentally by Ho and Gutmark [33], Kim and Samimy [11], and others. There is higher entrainment for the heated jet in all cases, from higher-velocity jets undergoing vigorous fine-scale mixing and leading to a shorter jet core length of almost $2D$ for both the rectangular and the circular jets (Fig. 12b). This conforms with the mixing noise dominance of the heated jets (Fig. 14b) being several decibels higher at all locations than the cold jets (Fig. 14a). From the $4D$ axial location, the rectangular jet mass entrainment gradually increases to $8D$: after which, there is no change in the slope, suggesting similar mixing characteristics as the circular jet and the absence of axis switching. The entrainment increases over the circular jet are approximately 1.35 and 1.2 for the cold and heated jets, respectively, at $9D$. This increase is driven by the large-scale streamwise vortices, as will be described next.



a) 0.5 (above) and 1.0D (below)



b) 2.0 and 3.0D

2. Vorticity

The dynamics of the coherent structures, their interactions, and the influence of incoherent turbulence can be gleaned to an extent from time-averaged data. Figures 16 and 17 show the evolution in the axial direction of the time-averaged streamwise velocity contour plots and the vorticity for the cold and heated rectangular jets. The velocity contours show the deformation of the rectangular exit cross section as it propagates downstream. Both cases have many features in common. The effects of mixing result in an outward spread of the contour lines at the sharp corners and an inward penetration at the edges. The corresponding time-averaged vorticity plots show the stretching of the azimuthal vortex ring into dominant streamwise vortices that exert their influence through a pair of counter-rotating vortices at each corner. The sense of rotation of the four vortex pairs results in movement of the fluid from the jet core toward the corners near the diagonal, as well as movement into the core along the edges away from the corners. The asymmetry in the spatial proximity of the vortex pairs upstream leads to stronger inflow at the minor axis side, as seen in Figs. 16b, 16c, 17b, and 17c. This leads to a contraction of the jet cross section, downstream, along the major axis, and leading to a more square shape of the outer velocity contours. The heated jets have a larger spreading rate and a faster dissipation rate of the streamwise components. This particular distribution of counter-rotating corner vortices with the specified inflow/outflow sense was

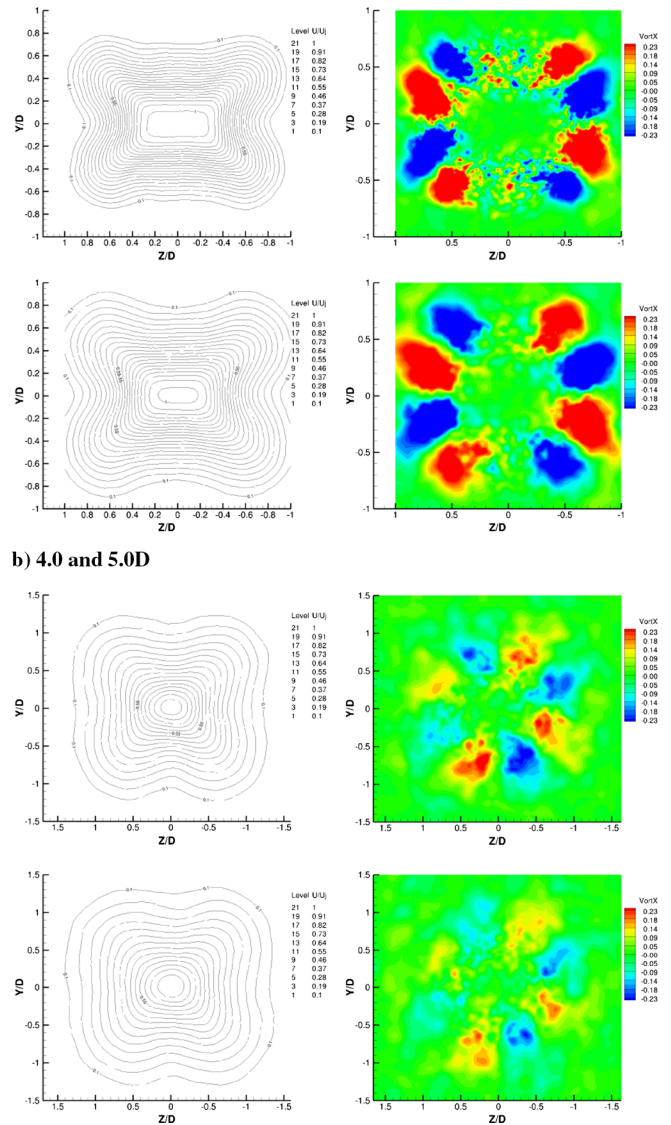


Fig. 17 Time-averaged velocity contours and axial vorticity for TR of 3.0. Plotted area changes are between $5.0D$ and $8.0D$.

not encountered in any of the experimental and computational cases in the reviewed literature.

The time-averaged plots show distinct streamwise components of the stretched azimuthal vortex ring at the corners past $3D$, and they affect the mixing until approximately $8D$ downstream. The strong self-induction at the corners and the resultant inflow/outflow causes the stretched coherent structures to approach the jet centerline as they convect downstream. Past $8D$, the effects of the corner vortices are absent, and the structures are similar to that seen in the circular jets without any time-averaged dominant streamwise components. Qualitatively, this can be seen from Fig. 18, which shows the instantaneous comparison of the vorticity and q -criterion isosurfaces for the nonheated circular and rectangular jets at ideal conditions to a streamwise distance of $8D$. Figure 18c shows an illustration of the possible evolution of the azimuthal vortex ring in the axial direction based on Figs. 16 and 17. Without instantaneous continuous tracking of the azimuthal vortex rings, it is unclear how far downstream the vortex maintains its coherence. The azimuthal vorticity ring devolves into stretched hairpin rings that create inflow and outflow in the cross-sectional plane, and this is reflected in the velocity contours. The sense of the induced inflow/outflow mixing setup by the vortex pairs in this instance inhibits any possibility of axis switching. Inflow happens at all sides and does not allow any one side to expand, which is a criteria for the switching to happen. The outflow that happens diagonally rounds out the sharp corners of the jet cross section. Past $6D$, the streamwise vorticity distribution is nearly axisymmetric; by $10D$, only weak streamwise components exist and the time-averaged flow is indistinguishable from a circular jet.

The higher mass entrainment for the rectangular jets, as seen in Fig. 15, corresponds to the same axial span over which the streamwise vortices have a role in the mixing. The large-scale stretching of the coherent azimuthal vortex at the corners differentiates the mixing features of the rectangular jet from the circular jet over that span. However, the noise between the heated jets (circular and rectangular) has minimal differences, as shown in Fig. 14b. The large-scale mixing with increased entrainment of the rectangular jet has minimal influence on the far-field noise.

3. Turbulence Intensities

The velocity fluctuations in the major and minor planes of the rectangular jets and in the center plane of the circular jets are shown in Figs. 19–22. Overall, for both the circular and the rectangular jets, the u' fluctuations are higher than v' and w' fluctuations in every cross-sectional plane in the axial direction.

In the cold jet, some of the turbulence intensities for the rectangular jet have a two-peak profile, with the peaks shifting based on the axial location. In the major plane, the peak u' turbulence shift is always toward the jet centerline; whereas in the minor plane, it shifts away with increasing streamwise distance. The first set of peaks is in line with the radial location of the respective lip lines, and the secondary set of aligned peaks for u' is located between $0.4D$ and $0.5D$ in both the major and minor planes. Note that u' has its maximal peak at $2D$, corresponding to where the jet plume spreading rate increases rapidly and the shear layers transition to turbulent flow. The centerline (line cut through $0D$ on the horizontal axis) u' intensity increases in the streamwise direction and reaches a peak at approximately $11D$. The other two turbulence intensity components follow similar trends. However, the peaks of v' and w' velocity fluctuations in the rectangular major plane are mostly along the lip line. In the minor axis plane, the peaks shift away from the centerline and converge to a similar radial distance as that seen in the major plane at approximately $0.6D$. At the axial location where the potential core of the rectangular cold jet ends, at about $8.1D$, there is a significant jump in the centerline turbulence of all three components. In contrast, the circular cold jet turbulence intensities display a very minimal shift in the peaks, and the peaks are offset away from the jet centerline. For all three circular jet components, the peaks are located radially at about $0.6D$, which is similar to the v' and w' peaks in the rectangular jet. Only the u' centerline turbulence of the circular jet shows a jump at the end of the potential core of around $9.6D$.

The heated jet turbulence intensity levels of all three components (v' and w' are not shown) are comparable to those of the rectangular and circular cold jets. The two distinct peaks in the rectangular cold jets are replaced with a more gradual shift of the peaks, especially in the u' turbulence profiles. The maximal peak, for most of the rectangular jets, happens at an axial location of $2D$, except for the v' minor plane and w' major plane, where it is at $3D$. With increased

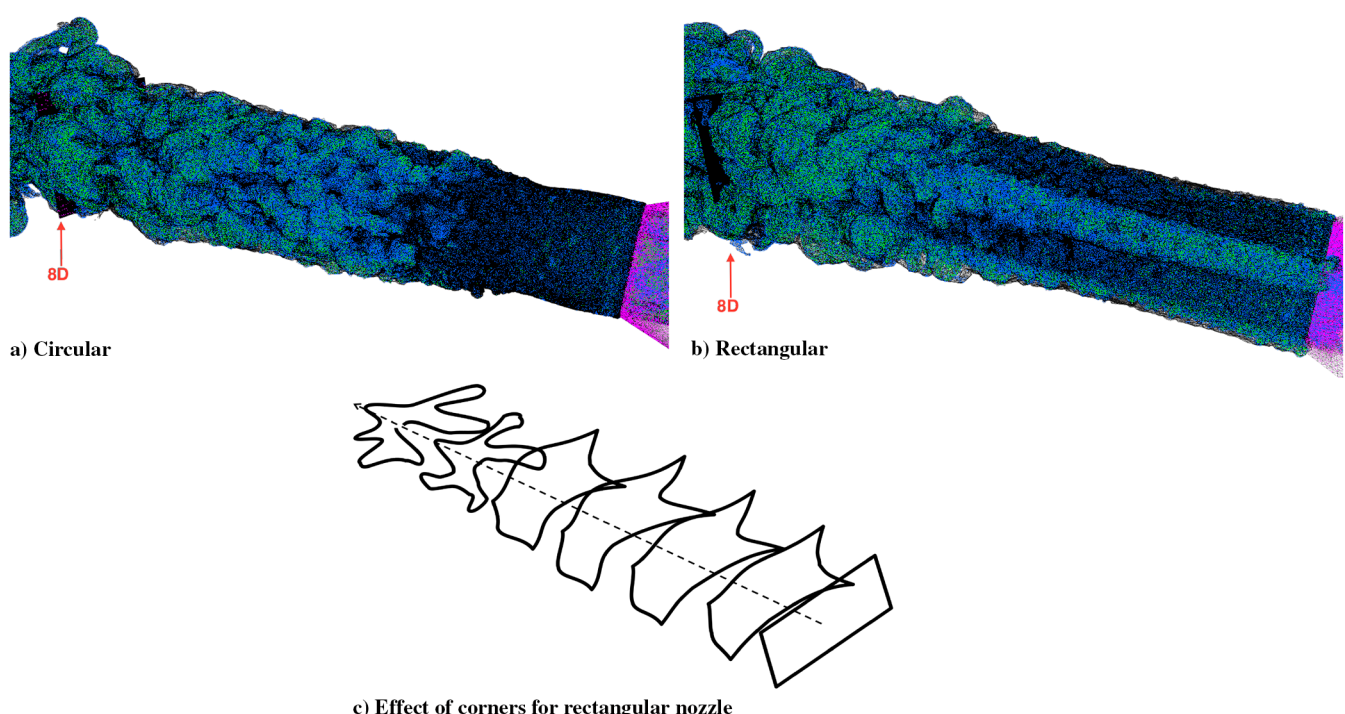


Fig. 18 Dynamics of the azimuthal vortex ring for circular and rectangular jets at TR of 1.0. Isosurfaces of vorticity and q criterion are shown to $8D$ axial distance. Jet direction is from right to left.

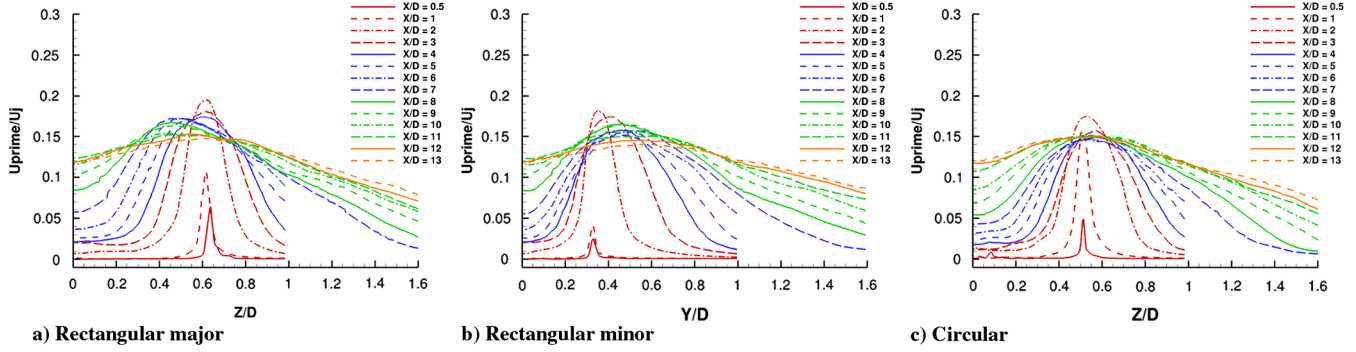


Fig. 19 Up prime for TR of 1.0.

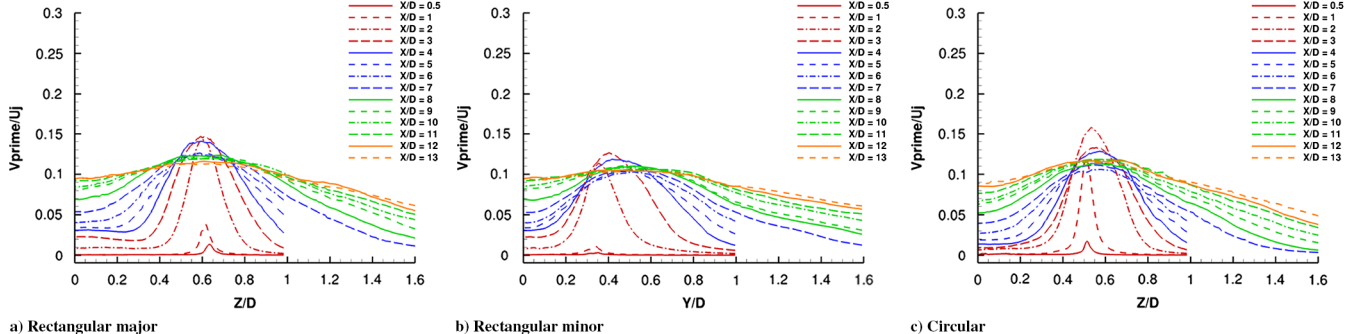


Fig. 20 V prime for TR of 1.0.

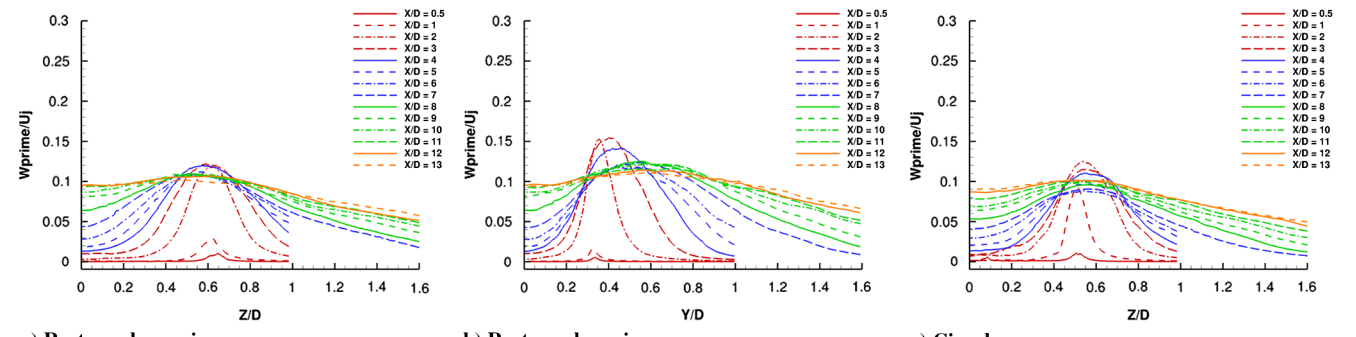


Fig. 21 W prime for TR of 1.0.

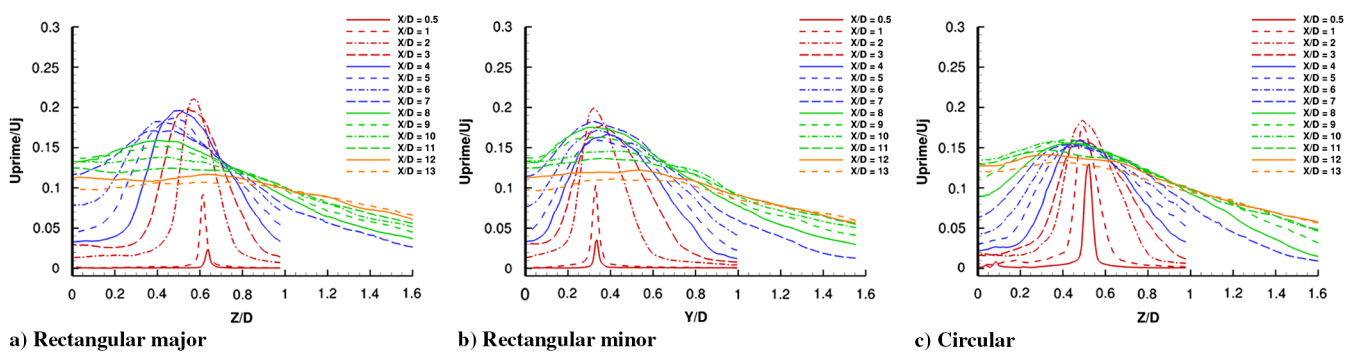


Fig. 22 Up prime for TR of 3.0.

mixing and shorter potential core lengths, the jet centerline turbulence intensity profiles are different in the heated cases. The intensities of all three components peak at streamwise distance of $9D$. At the centerline locations of approximately $6D$ in the rectangular jet and $8D$ in the circular jet, where the potential core ends, there is a jump in u' turbulence intensity. Similar to the cold jets, the circular jet turbulence intensities show a very minimal shift

in the peaks with a streamwise distance, and they are all located along the lip line.

The shifting of the peaks stand out as the major difference between the circular and rectangular jet turbulence intensity profiles. The primary factors are the regions of induced inflow and outflow around the jet centerline due to the azimuthal vortex ring streamwise deformation in the rectangular jets. As seen before in the velocity

contours, this affects mixing characteristics along both the major and minor axes. These occur until approximately $8.0D$, after which the turbulence intensity profiles are similar and converge in both the major and minor axis planes to have a more axisymmetric distribution. Despite the differences in the velocity fluctuation profiles in the streamwise direction between rectangular and circular jets, potentially affecting their respective noise generation, for heated jets, the rectangular and circular far-field OASPLs overlap; whereas they differ for the cold jets (Fig. 14). Any obvious causal relation to the far-field noise is absent.

VII. Conclusions

The noise generated, at a specified far-field distance, by a supersonic rectangular jet with an aspect ratio two was compared with that generated by a circular jet of equivalent diameter and the same design Mach number. This was done at two operating temperature ratios at the ideally expanded condition. Validation results for both nozzle geometries were shown for the cold and heated jets with good agreement.

Using the simulation data, flow features are compared between the rectangular and the circular jets. The plume spread of the circular jet and the major and minor planes of the rectangular jet differ slightly near the nozzle exit but converge soon after to a common spreading rate with minimal deviation. However, the shock cell structures have significant differences between the planes in terms of shock cell size, location, rate of decay, and the type of shocks. The double-diamond shock cells are present in both the minor axis plane of the rectangular jet and the circular jet. It is absent in the major axis plane. These differences translate to significant difference of more than 5 dB in the noise profile between the circular and rectangular cold jets, as seen in the SPL noise spectra at various observer locations upstream. The cold circular jet OASPL is higher, by up to 3.5 dB, than the rectangular jet at various upstream and downstream locations. When the operating temperature is increased, the shock cell structures remain unaffected near the nozzle exit but the cells decay faster, showing a weak dependence on the temperature. The shock-associated noise contribution to the overall noise decreases, and the circular and rectangular jet SPL profiles overlap at the sideline locations and deviate minimally at the extreme upstream and downstream locations. The OASPL levels are within 2 dB in all three planes for the heated jets.

Examining jet streamwise velocity distributions in each plane at equivalent radial distances (normalized based on the distance of the lip from the jet centerline), no similarity in flow characteristics are observed. For a given temperature, the jet potential core lengths differ between the circular and rectangular jets; the rectangular jet core is shorter due to the higher mixing and entrainment of the rectangular jets. The time-averaged streamwise velocity and vorticity plots at various cross-sectional planes show that there is strong self-induction and stretching of the large-scale coherent azimuthal structures, especially at the corners, that differentiate the mixing features of the rectangular from the circular jet. The streamwise vorticity dynamics are affected by the variation of the self-induction of the azimuthal vortex ring around the rectangular nozzle lip. For the same aspect ratio nozzle at two different operating temperatures, a similar spatial distribution of streamwise counter-rotating vortex pairs is seen at each corner. The rotational influence of the vortex pairs at the corners acts such that it inherently inhibits axis switching downstream through the induced inflow at all sides and induced outflow only diagonally along the corners. Interestingly, this particular distribution of four vortex pairs with the specified rotational sense was not encountered in any of the reviewed literature cases. The streamwise vortices are not sustained past $8.0D$, and the time-averaged vorticity around the jet centerline takes on a more axisymmetric profile, which is similar to a circular jet. The influence of the large-scale vorticity dynamics are seen in the turbulence intensity profiles in the major and minor planes for the rectangular jets. In the absence of axis switching, the overall turbulence intensity levels are similar between the circular and rectangular jets.

Despite the differences recorded in the flowfield characteristics between the rectangular and circular jets, these differences have a minimal direct influence on the far-field noise within the scope of the cases considered here. The large-scale mixing due to streamwise vortices, with increased entrainment, is present in both cold and heated rectangular jets. The far-field noise, on the other hand, is practically overlapping for the rectangular and circular heated jets; whereas the differences in the cold jets are more due to the shock contribution level.

Acknowledgments

This research has been sponsored by the Office of Naval Research through the Jet Noise Reduction Program, as well as the Naval Research Laboratory 6.1 Base Program. Computing resources were provided by the U.S. Department of Defense High Performance Computing Modernization Program Office. The authors would like to thank Junhui Liu at the Naval Research Laboratory for all of her advice on the computational work presented in the paper.

References

- [1] Henderson, B., "Fifty Years of Fluidic Injection for Jet Noise Reduction," *International Journal of Aeroacoustics*, Vol. 9, Nos. 1–2, 2010, pp. 91–122.
doi:10.1260/1475-472X.9.1-2.91
- [2] Tam, C. K. W., "Supersonic Jet Noise," *Annual Review of Fluid Mechanics*, Vol. 27, No. 1, 1995, pp. 17–43.
doi:10.1146/annurev.fl.27.010195.000313
- [3] Hiley, P. E., Wallace, H. W., and Booz, D. E., "Nonaxisymmetric Nozzles Installed in Advanced Fighter Aircraft," *Journal of Aircraft*, Vol. 13, No. 12, Dec. 1976, pp. 1000–1006.
doi:10.2514/3.58740
- [4] Sato, H., "The Stability and Transition of a Two-Dimensional Jet," *Journal of Fluid Mechanics*, Vol. 7, No. 1, April 1959, pp. 53–79.
doi:10.1017/S0022112060000049
- [5] Sforza, P. M., Steiger, M. H., and Trentacoste, N., "Studies on Three-Dimensional Viscous Jets," *AIAA Journal*, Vol. 4, No. 5, 1966, pp. 800–806.
doi:10.2514/3.3549
- [6] Kantola, R. A., "Noise Characteristics of Heated High Velocity Rectangular Jets," *Journal of Sound and Vibration*, Vol. 64, No. 2, 1979, pp. 277–294.
doi:10.1016/0022-460X(79)90652-7
- [7] Krothapalli, A., Baganoff, D., and Karamcheti, K., "On the Mixing of a Rectangular Jet," *Journal of Fluid Mechanics*, Vol. 107, June 1981, pp. 201–220.
doi:10.1017/S0022112081001730
- [8] Husain, H. S., and Hussain, A. K. M. F., "Controlled Exciting of Elliptic Jets," *Physics of Fluids A*, Vol. 26, No. 10, Oct. 1983, pp. 2763–2766.
doi:10.1063/1.864062
- [9] Grinstein, F., "Vorticity Dynamics in Spatially Developing Rectangular Jets," *3rd Shear Flow Conference*, AIAA Paper 1993-3286, May 1993.
- [10] Gutmark, E., Schadow, K. C., and Bicker, C. J., "Near Acoustic Field and Shock Structure of Rectangular Supersonic Jets," *AIAA Journal*, Vol. 28, No. 7, 1990, pp. 1163–1170.
doi:10.2514/3.25187
- [11] Kim, J. H., and Samimy, M., "Mixing Enhancement via Nozzle Trailing Edge Modifications in a High Speed Rectangular Jet," *Physics of Fluids*, Vol. 11, No. 9, Sept. 1999, pp. 2731–2742.
doi:10.1063/1.870132
- [12] Zaman, K. B. M., "Axis Switching and Spreading of an Asymmetric Jet: The Role of Coherent Structure Dynamics," *Journal of Fluid Mechanics*, Vol. 316, June 1996, pp. 1–27.
doi:10.1017/S0022112096000420
- [13] Gutmark, E. J., and Grinstein, F. F., "Flow Control with Noncircular Jets," *Annual Review of Fluid Mechanics*, Vol. 31, No. 1, 1999, pp. 239–272.
doi:10.1146/annurev.fluid.31.1.239
- [14] Krothapalli, A., "Discrete Tones Generated by an Impinging Underexpanded Rectangular Jet," *AIAA Journal*, Vol. 23, No. 12, Dec. 1985, pp. 1910–1915.
doi:10.2514/3.9195
- [15] Raman, G., and Rice, E., "Instability Modes Excited by Natural Screech Tones in a Supersonic Rectangular Jet," *15th AIAA Aeroacoustics Conference*, AIAA Paper 1993-4321, 1993.

- [16] Kolbe, R., Kailasanath, K., Young, T., Boris, J., and Landsberg, A., "Numerical Simulations of Flow Modification of Supersonic Rectangular Jets," *AIAA Journal*, Vol. 34, No. 5, 1996, pp. 902–908. doi:10.2514/3.13166
- [17] Kerechanin, C. W., Samimy, M., and Kim, J. H., "Effects of Nozzle Trailing Edges on Acoustic Field of Supersonic Rectangular Jet," *AIAA Journal*, Vol. 39, No. 6, June 2001, pp. 1065–1070. doi:10.2514/2.1418
- [18] Goss, A. E., Veltin, J., and McLaughlin, D. K., "Acoustic Measurements of High-Speed Jets from Rectangular Nozzle with Thrust Vectoring," *AIAA Journal*, Vol. 47, No. 6, June 2009, pp. 1482–1490. doi:10.2514/1.39843
- [19] Veltin, J., and McLaughlin, D. K., "Flow Field and Acoustic Measurements of Rectangular Supersonic Jets," *47th AIAA Aerospace Sciences Meeting*, AIAA Paper 2009-0019, Jan. 2009.
- [20] Tipnis, T. J., "Effects of Upstream Nozzle Geometry on Rectangular Free Jets," Ph.D. Thesis, Cranfield Univ., Cranfield, England, U.K., July 2010.
- [21] Heeb, N., Mora, P., Gutmark, E., and Kailasanath, K., "Investigation of the Noise from a Rectangular Supersonic Jet," *19th AIAA/CEAS Aeroacoustics Conference*, AIAA Paper 2013-2239, May 2013.
- [22] Mora, P., Baier, F., Gutmark, E. J., and Kailasanath, K., "Acoustics from a Rectangular C-D Nozzle Exhausting over a Flat Surface," *54th AIAA Aerospace Sciences Meeting*, AIAA Paper 2016-1884, Jan. 2016.
- [23] Corrigan, A., Kailasanath, K., Liu, J., Ramamurti, R., Schwer, D., and Dahm, J., "A Hybrid Grid Compressible Flow Solver for Large-Scale Supersonic Jet Noise Simulation on Multi-GPU Clusters," *50th AIAA Aerospace Sciences Meeting Including the New Horizons Forum and Aerospace Exposition*, AIAA Paper 2012-0564, 2012, pp. 1–6.
- [24] Kailasanath, K., Corrigan, A., Liu, J., and Ramamurti, R., "Efficient Supersonic Jet Noise Simulations Using JENRE," *50th AIAA/ASME/SAE/ASEE Joint Propulsion Conference*, AIAA Paper 2014-3740, June 2014.
- [25] Luo, H., Baum, J., and Löhner, R., "Edge Based Finite Element Scheme for the Euler Equations," *AIAA Journal*, Vol. 32, No. 6, 1994, pp. 1183–1190. doi:10.2514/3.12118
- [26] Boris, J. P., and Book, D. L., "Flux-Corrected Transport I: SHASTA a Fluid Transport Algorithm that Works," *Journal of Computation Physics*, Vol. 11, No. 1, 1973, pp. 38–69. doi:10.1016/0021-9991(73)90147-2
- [27] Kuzmin, D., Möller, M., and Gurris, M., "Algebraic Flux Correction II: Compressible Flow Problems," *Flux-Corrected Transport: Principles, Algorithms, and Applications*, edited by D. Kuzmin, and R. Löhner, Springer, New York, 2012, pp. 193–238.
- [28] Löhner, R., Morgan, K., Peraire, J., and Vahdati, M., "Finite Element Flux-Corrected Transport (FEM-FCT) for the Euler and Navier-Stokes Equations," *International Journal for Numerical Methods in Fluids*, Vol. 7, No. 10, 1987, pp. 1093–1109.
- [29] Löhner, R., *Applied CFD Techniques*, Wiley, New York, 2008, pp. 238–251.
- [30] Williams, J. E. F., and Hawkings, D. L., "Sound Generation by Turbulence and Surfaces in Arbitrary Motion," *Philosophical Transactions of the Royal Society of London, Series A: Mathematical and Physical Sciences*, Vol. 264, No. 1151, May 1969, pp. 321–342. doi:10.1098/rsta.1969.0031
- [31] Liu, J., Corrigan, A. T., Kailasanath, K., Heeb, N. S., and Gutmark, E. J., "Numerical Study of Noise Characteristics in Overexpanded Jet Flows," *53rd AIAA Aerospace Sciences Meeting*, AIAA Paper 2015-0508, May 2015.
- [32] Koshigoe, S., Gutmark, E. J., Schadow, K. C., and Tubis, A., "Initial Development of Noncircular Jets Leading to Axis Switching," *AIAA Journal*, Vol. 27, No. 4, April 1989, pp. 411–419. doi:10.2514/3.10128
- [33] Ho, C.-M., and Gutmark, E., "Vortex Induction and Mass Entrainment in a Small-Aspect-Ratio Elliptic Jet," *Journal of Fluid Mechanics*, Vol. 179, June 1987, pp. 383–405. doi:10.1017/S0022112087001587
- [34] Gutmark, E., Schadow, K. C., and Wilson, K. J., "Effect of Convective Mach Number on Mixing of Coaxial Circular and Rectangular Jets," *Physics of Fluids*, Vol. 3, No. 1, Jan. 1991, pp. 29–36. doi:10.1063/1.857860
- [35] Grinstein, F., "Vortex Dynamics and Entrainment in Rectangular Free Jets," *Journal of Fluid Mechanics*, Vol. 437, June 2001, pp. 69–101. doi:10.1017/S0022112001004141

D. Papamoschou
Associate Editor